Quasiparticle and excitonic properties of monolayer $SrTiO_3$

Lorenzo Varrassi,[1,*] Peitao Liu,[2] and Cesare Franchini[1,3]

[1]*Dipartimento di Fisica e Astronomia, Universitá di Bologna, 40127 Bologna, Italy*

[2]*Shenyang National Laboratory for Materials Science, Institute of Metal Research, Chinese Academy of Sciences, Beijing 110016, China*

[3]*Faculty of Physics and Center for Computational Materials Science, University of Vienna, Kolingasse 14-16, A-1090, Vienna, Austria*

(Received 20 June 2023; revised 7 November 2023; accepted 8 January 2024; published 7 February 2024)

$SrTiO_3$ is one of the most studied transition metal oxides. Recently, a breakthrough was achieved with the fabrication of freestanding $SrTiO_3$ ultrathin films down to the monolayer limit. However, the many-body effects on the quasiparticle and optical properties of monolayer $SrTiO_3$ remain unexplored. Using state-of-the-art many-body perturbation theory in the GW approximation combined with the Bethe-Salpeter equation, we study the quasiparticle band structure, optical, and excitonic properties of monolayer $SrTiO_3$. We show that quasiparticle corrections significantly alter the band-structure topology; however, the widely used diagonal G_0W_0 approach yields unphysical band dispersions. The correct band dispersions are restored only by taking into account the off-diagonal elements of the self-energy. The optical properties are studied both in the optical limit and for finite momenta by computing the electron energy loss spectra. We find that the imaginary part of two-dimensional polarizability at the long wavelength limit is dominated by three strongly bound excitonic peaks and the direct optical gap is associated to a bright exciton state with a large binding energy of 0.93 eV. We discuss the character of the excitonic peaks via the contributing interband transitions and reveal that the lowest bound excitonic state becomes dark for finite momenta along Γ-M, while the other two excitonic peaks disperse to higher energies and eventually merge for momenta close to M.

DOI: 10.1103/PhysRevMaterials.8.024001

I. INTRODUCTION

Transition metal oxide (TMO) perovskites have attracted wide interest in the last years due to the many intriguing physical properties and possible technological applications in various fields as oxide electronics, spintronic, or catalysis [1–4]. Among them $SrTiO_3$ has acquired a prototypical role: it's one of the most studied perovskites and has been employed as a proving ground to propose or compare different computational schemes [5,6], including many-body *ab initio* methods [7–11] and machine-learning based algorithms [12,13]. The impact of its electronic structure on the conducting, magnetic, and optical properties has been widely investigated, and intriguing phenomena such as superconductivity or two-dimensional electron gas [14,15] have been identified and analyzed. In particular, several theoretical works [8–10,16] analyzed the role of electronic correlations and localized d states in the optical response, and highlighted how including an explicit description of excitonic interactions is necessary to achieve a satisfactory agreement with the experimental data. Recently, an important breakthrough was achieved by Ji *et al.* [17] through the synthesis of freestanding two-dimensional (2D) perovskites $SrTiO_3$ and $BiFeO_3$ films with a thickness reaching the monolayer limit. Their work proves that TMO perovskite films can be realized with thicknesses below the critical limit previously proposed as necessary for crystalline order stability [18]. A year later, freestanding $PbTiO_3$ films were fabricated with thicknesses down to four unit cells by Han *et al.* [19]. These results sparked notable interest towards ultrathin perovskites [20] and prompted a series of experimental and theoretical works aimed at exploring their structural, electronic [21–29] and mechanical properties [19,30,31]. Superelasticity was identified in $BaTiO_3$ [32], while the presence of a ferroelectric transition was recognized in $SrTiO_3$ and $PbTiO_3$ 2D compounds [19,33,34]. Another line of research investigated how the electronic properties can be tuned by engineering strain or employing heterostructures approaches [35–38]. Nevertheless, to the best of our knowledge, a comprehensive study of the excitonic and optical properties of $SrTiO_3$ in the monolayer limit has not been discussed yet in literature. Low-dimensional systems have been intensely studied due to their fascinating optical and excitonic physics: these systems exhibit a significantly enhanced electron-hole interaction, stemming from substantially reduced nonlocal screening when compared to their bulk counterparts [39–50]. Furthermore, excitonic effects dominate the optical response and lead to binding energies exceeding those found in bulk semiconductors up to one order of magnitude [47,51,52]. The experimental synthesis of freestanding TMO perovskites monolayer presents therefore the opportunity to expand this analysis from the bulk phases to 2D structures. In this work we present a first-principles study of the optical spectra and the underlying excitonic transitions of monolayer $SrTiO_3$, determined through the solution of the Bethe-Salpeter equation (BSE), where the quasiparticle (QP) eigenstates and screened Coulomb interactions are computed by the GW method. Our simulations indicate that DFT with semi-local

*Corresponding author: lorenzo.varrassi3@unibo.it

functionals predicts incorrect hybridizations between Ti-d and O-2p orbitals for the lower conduction bands, thus yielding incorrect band characters. This leads to a severe failure for the diagonal G_0W_0 method when taking semi-local DFT energies and orbitals as a starting point. Taking into account the off-diagonal self-energy elements allows to restore the correct band dispersions at GW level and describe the correct hybridizations of the conduction bands. Furthermore, recent studies [21,26] on the SrO-terminated monolayer structure using the HSE06 [53] and GGA + U approaches report a conflicting description of the conduction bands character, which differs depending on the functional employed. Our study contributes therefore to address the shortcoming of the HSE06 functional and the role of nonlocal contributions. Moreover, we find that excitonic effects significantly alter the optical spectra. Reduced dimensionality effects induce a considerable enhancement of exciton binding energies with respect to the bulk phase, yielding a binding energy as large as 0.93 eV for the first excitonic state. In addition to the spectral weight transfer visible also in bulk, new bound exciton peaks appear in monolayer $SrTiO_3$; the origin of these excitonic peaks is clarified by analyzing the coupling components of the BSE eigenstates associated to these peaks.

II. METHODS AND COMPUTATIONAL DETAILS

Our calculations were performed using the VASP software [54,55], with the GW versions of the projector augmented wave (PAW) potentials [56,57]; the norm-conserving PAW were used for Sr and Ti [8]. The QP band structures were computed using the *ab initio* G_0W_0 method [58–60]. In many-body perturbation theory, the QP wave functions and eigenvalues are determined by a Schrödinger-like equation involving the self-energy Σ:

$$[T + V_H + V_{\text{ext}}]\phi^{\text{QP}}_{n\mathbf{k}}(\mathbf{r}) + \int \Sigma(\mathbf{r}, \mathbf{r}', \omega')\phi^{\text{QP}}_{n\mathbf{k}}(\mathbf{r}')d\mathbf{r}' = E^{\text{QP}}_{n\mathbf{k}}\phi^{\text{QP}}_{n\mathbf{k}}(\mathbf{r}), \quad (1)$$

where T is the kinetic term, V_{ext} is the external potential, and V_H is the Hartree potential; the self-energy operator Σ in the G_0W_0 approximation is given by

$$\Sigma(\mathbf{r}, \mathbf{r}', \omega') = \frac{i}{2\pi}\int_{-\infty}^{\infty} G_0(\mathbf{r}, \mathbf{r}', \omega + \omega') \times W_0(\mathbf{r}, \mathbf{r}', \omega')e^{i\omega' 0^+}d\omega', \quad (2)$$

where the screened interaction W_0 and the Green function G_0 are calculated from the DFT one-electron energies and orbitals, and W_0 is determined by the random phase approximation (RPA). Two different G_0W_0 schemes are discussed through this work. In the $G_0W_0^{\text{full}}$ approach the Hamiltonian is constructed starting from the full self-energy matrix expressed on the basis of DFT states $\langle\phi^{\text{DFT}}_{n\mathbf{k}}|\,\Sigma\,|\phi^{\text{DFT}}_{m\mathbf{k}}\rangle$ [61–64]. The scheme employed is described in Ref. [61]: in the first step the self-energy is linearized around the DFT energy and the equation is recast as a generalized (non-Hermitian) eigenvalue problem

$$\underbrace{\left[T + V + \Sigma\left(E^{\text{DFT}}_{n\mathbf{k}}\right) - \xi\left(E^{\text{DFT}}_{n\mathbf{k}}\right)E^{\text{DFT}}_{n\mathbf{k}}\right]}_{H(E^{\text{DFT}}_{n\mathbf{k}})}\left|\phi^{\text{QP}}_{n\mathbf{k}}\right\rangle = E_{n\mathbf{k}}\underbrace{\left[1 - \xi\left(E^{\text{DFT}}_{n\mathbf{k}}\right)\right]}_{S(E^{\text{DFT}}_{n\mathbf{k}})}\left|\phi^{\text{QP}}_{n\mathbf{k}}\right\rangle, \quad (3)$$

with $\xi(E_{n\mathbf{k}}) = \frac{\partial\Sigma(E_{n\mathbf{k}})}{\partial E_{n\mathbf{k}}}$. In the second step, the Hermitian part of the Hamiltonian and of the overlap matrix S are determined

$$H_h = \tfrac{1}{2}(H + H^\dagger), \quad S_h = \tfrac{1}{2}(S + S^\dagger). \quad (4)$$

The QP wave functions and eigenvalues are then determined by diagonalizing the corresponding Hermitian eigenvalue problem

$$S_h{}^{-1/2}H_hS_h{}^{-1/2}U = U\Lambda, \quad (5)$$

where Λ is the diagonal eigenvalue matrix and U is a unitary matrix. The QP wave functions are given by $\phi^{\text{QP}}_{n\mathbf{k}} = \sum_m U_{mn}\phi^{\text{DFT}}_{m\mathbf{k}}$. The off-diagonal elements are computed for a subspace spanned by the first 64 bands. The second one is the widely used one-shot approach based on the diagonal approximation of the self-energy Σ, referred to as $G_0W_0^{\text{diag}}$:

$$E^{\text{QP}}_{n\mathbf{k}} = E^{\text{DFT}}_{n\mathbf{k}} + Z_{n\mathbf{k}}\left\langle\phi^{\text{DFT}}_{n\mathbf{k}}\right|\Sigma\left(E^{\text{DFT}}_{n\mathbf{k}}\right) - V_{xc}\left|\phi^{\text{DFT}}_{n\mathbf{k}}\right\rangle, \quad (6)$$

where $Z_{n\mathbf{k}}$ is the renormalization factor

$$Z_{n\mathbf{k}} = \left[1 - Re\left(\left\langle\phi^{\text{DFT}}_{n\mathbf{k}}\right|\frac{\partial\Sigma\left(E^{\text{DFT}}_{n\mathbf{k}}\right)}{\partial\omega}\left|\phi^{\text{DFT}}_{n\mathbf{k}}\right\rangle\right)\right]^{-1}. \quad (7)$$

This approach implicitly assumes that the matrix elements $\langle\phi^{\text{DFT}}_{n\mathbf{k}}|\,\Sigma - V_{xc}\,|\phi^{\text{DFT}}_{m\mathbf{k}}\rangle$ are band diagonal. A $24 \times 24 \times 1$ k-point mesh guaranteed a convergence of the QP and optical direct gaps of ∼0.05 eV, and a vacuum region of 40 Å along the direction perpendicular to the monolayer was introduced to avoid spurious interactions with the periodic images. The vacuum width of 40 Å was established through a convergence study on the $G_0W_0^{\text{diag}}$ QP gaps with a convergence threshold of 0.05 eV. Ninety-six frequency points were employed to represent the screened potential and the self-energy. The convergence study for the energy cutoff and the number of empty bands was carried out using the $G_0W_0^{\text{diag}}$ scheme. The interdependence of these parameters [65–67] was taken into account by employing a standard convergence framework [11]: the direct and indirect gaps were evaluated as a function of the number of bands at a constant energy cutoff (the number of bands did not exceed the maximum number of plane waves compatible with the given cutoff), and then the procedure was repeated for several cutoff values. To achieve a convergence of the QP gaps within ∼0.03 eV it was necessary to employ 2200 empty bands and a cutoff of 600 eV (with an energy cutoff for the response function set at 325 eV). In contrast, utilizing the same energy cutoffs, the inclusion of 1100 bands only results in a convergence of 0.10 eV for the QP gaps. To reduce the expensive computational cost of the $G_0W_0^{\text{full}}$ simulation, the $G_0W_0^{\text{full}}$ results were obtained with the inclusion of 192 bands and finite basis errors were corrected through the introduction of a scissor operator. The scissor shift was determined as the

difference between the QP direct gaps of two $G_0W_0^{diag}$ calculations using a different number of bands: in the first one 192 empty bands were used to calculate the screened potential and self-energy, while the second one was conducted with the converged value of 2200 bands. Both runs maintained a 600 eV energy cutoff, 40 Å vacuum, and a $24 \times 24 \times 1$ k-point mesh. To further accelerate the computation, the $G_0W_0^{diag}$ runs were performed within the plasmon pole model [58,68] and the GPU version of the YAMBO software [69,70]. The full computational details regarding the convergences and the YAMBO setup are compiled in the Supplemental Material [71] (see also Refs. [72,73] therein). The optical properties were calculated by solving the (momentum-dependent) Bethe-Salpeter equation (BSE) [74–76]:

$$H^{\text{exc}}(\mathbf{q})\,|\Lambda,\mathbf{q}\rangle = E^{\Lambda}(\mathbf{q})\,|\Lambda,\mathbf{q}\rangle\,, \tag{8}$$

$$|\Lambda,\mathbf{q}\rangle = \sum_{v,c}\sum_{\mathbf{k}} A^{\Lambda}_{vc\mathbf{k}}(\mathbf{q})\,|v,\mathbf{k}-\mathbf{q}\rangle\,|c,\mathbf{k}\rangle\,, \tag{9}$$

where $E^{\Lambda}(\mathbf{q})$ and $A^{\Lambda}_{vc\mathbf{k}}$ are the BSE eigenvalues and eigenvectors amplitudes, and v, c refer to the valence and conduction bands. The equation was solved within the Tamm-Dancoff approximation [75], including eight valence and ten conduction bands. The static screened Coulomb matrix elements used to build the BSE kernel were recalculated separately with the inclusion of 1100 bands. The response function $\chi_{\mathbf{G}=0,\mathbf{G}'=0}$ with the inclusion of excitonic effects is defined as

$$\chi_{00}(\mathbf{q}\to 0,\omega) = 2\lim_{\mathbf{q}\to 0}\sum_{\Lambda}\frac{|\sum_{v,c,\mathbf{k}} A^{\Lambda}_{vc\mathbf{k}}(\mathbf{q})\rho_{v\mathbf{k}c\mathbf{k}+\mathbf{q}}|^2}{\omega - E^{\Lambda} + i\eta}, \tag{10}$$

where η is a positive infinitesimal and the transition matrix elements ρ are defined as $\rho_{v\mathbf{k}c\mathbf{k}+\mathbf{q}} = \langle c,\mathbf{k}+\mathbf{q}|\,e^{i\mathbf{q}\cdot\mathbf{r}}\,|v,\mathbf{k}\rangle$. The key quantity linked with the optical absorption in 2D systems is the 2D polarizability [77]

$$\alpha(\omega) = -\lim_{\mathbf{q}\to 0}\frac{L}{4\pi}\frac{1}{\mathbf{q}^2}\chi_{00}(\mathbf{q},\omega), \tag{11}$$

where L is the size of the cell in the nonperiodic direction.

III. RESULTS AND DISCUSSION

The geometry of the stoichiometric monolayer $SrTiO_3$ (001) was determined through a structural optimization starting from the relaxed cubic bulk phase. The optimization results in distortions along the z axis [see Fig. 1(b)], in agreement with previous works [22,78]: The Ti and Sr atoms are displaced toward the inner side, with a larger displacement associated to the Sr atom, corresponding to the $C4v$ symmetry group. The dynamical stability of the relaxed cell is validated by the stable phonon spectra reported in Ref. [22]. Furthermore, the absence of any imaginary frequency was confirmed in a subsequent study conducted by Juraschek *et al.* [79]. The distortions give rise to a polarization perpendicular to the monolayer plane [22] (see Fig. 1), which was calculated to be 0.069 $|e|$Å using the Berry phase method [80]. This value is consistent with the one estimated by the approximated expression $\mathbf{P}_{\text{tot}} = \sum_i \Delta R_i Z_i^*$ (where ΔR_i are the atomic displacements and Z_i the Born effective charges) which gives 0.062 $|e|$Å.

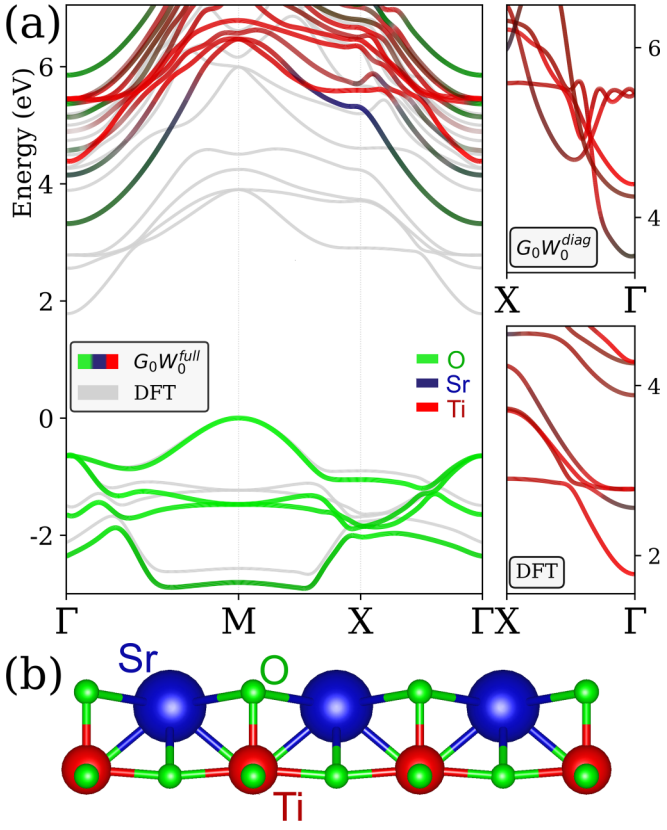

FIG. 1. (a) DFT (grey lines) and orbital-projected $G_0W_0^{full}$ band structures. Colors represent the O (green), Ti (red), and Sr (blue) characters, respectively, The two right panels show the orbital-projected unoccupied bands along X-Γ calculated by $G_0W_0^{diag}$ and DFT. (b) Stoichiometric monolayer $SrTiO_3$ structure.

A. Electronic properties

To obtain accurate optical properties, an accurate description of the QP band structures is indispensable [81]. Remarkably, the QP corrections for monolayer $SrTiO_3$ are not just rigid energy shifts, but rather prove to be k-point and band-dependent. As displayed in Fig. 1, the DFT band structure shows markedly different conduction bands dispersion with respect to $G_0W_0^{full}$ predicted ones: this difference is connected to an inadequate description of orbital characters by DFT with semi-local functional.

In the DFT band structure [grey lines in Fig. 1(a)] the conduction manifolds are dominated by Ti-d states; by contrast, the conduction manifolds predicted by $G_0W_0^{full}$ exhibit a sizable hybridization between Ti-d and Sr and O-p states. In particular, the lowest conduction band possesses a considerable mixing of Sr states (up to ∼40%) and O-p (up to ∼20%) along Γ-M and X-Γ. The valence bands characters are unchanged between $G_0W_0^{full}$ and DFT and are clearly contributed by the O-p states. In fact the QP valence bands can be successfully modeled using a typical scissor plus stretching correction.

It is instructive to compare these results with the widely used diagonal G_0W_0 approximation. Since the $G_0W_0^{diag}$ method retains a pronounced starting point dependence [74,82–85], it is not so surprising that $G_0W_0^{diag}$ on top of

TABLE I. Direct and indirect QP and optical gaps for the monolayer and bulk $SrTiO_3$. Both $G_0W_0^{full}$ and $G_0W_0^{diag}$ predicted QP gaps are shown. The optical gaps and the associated exciton binding energies E_{xb} for the monolayer structure are determined by solving the Bethe-Salpeter equation starting from $G_0W_0^{full}$ predicted QP eigenstates. The data for the bulk phase are from Refs. [8,11].

	Monolayer		Bulk	
	Dir.	Ind.	Dir.	Ind.
BSE@G_0W_0	3.588	2.891	3.73[8]	-
E_{xb}	0.93	0.98	0.21[8]	-
$G_0W_0^{full}$	4.514	3.870	-	-
$G_0W_0^{diag}$	4.743	4.099	3.94[11]	3.55[11]
DFT	2.427	1.781	2.23	1.86

the incorrect DFT band characters results in unphysical band dispersions and multiple crossings long X-Γ among the lower conduction bands [see Fig. 1(a)]. The failure of $G_0W_0^{diag}$ originates from the neglect of off-diagonal matrix elements of the self-energy: the full self-energy operator correctly couples the single particle Kohn-Sham orbitals and restores the correct hybridizations, thus avoiding the multiple band crossings [see Fig. 1(a)]. Similar behaviors were observed in several bulk materials, such as topological insulators [86–88] and compounds with strong p-d hybridizations [89–92]. However, only a very limited number of works in literature on 2D materials [93] report such a significant impact of the off-diagonal Σ terms. A valuable example is the study of Förster *et al.* [93], which points out that the omission of off-diagonal Σ elements results in non-physical features in the GW band structure of few-layer Sb_2Te_3 and Bi_2Se_3. The crucial effect of the Σ operator beyond the diagonal approximation has never been reported for 2D transition metal oxides and never in the monolayer limit. Moreover, recent studies based on the HSE06 functional [26] and the GGA + U approach [21] of the SrO-terminated $SrTiO_3$ monolayer provide a conflicting description on the conduction band minimum (CBM) band character. The GGA + U introduces a contribution of Sr 5s states to the CBM, while the HSE06 determines a CBM predominantly formed by Ti-d states. Likewise, the HSE06 functional applied to the stoichiometric monolayer (discussed in this work) depicts a CBM characterized by minimal hybridization, closely resembling the DFT description, and therefore, is not able to cure the nonphysical dispersions when used as a starting point for $G_0W_0^{diag}$ (see SI Fig. 3). By increasing the short range Fock exchange fraction α the HSE scheme is able to reproduce the CBM hybridized character (although the corresponding HSE band structure reproduces only partially the GW one, see SI Fig. 5). This behavior can be clarified by recalling that the short-range exchange fraction α can be related to the screening properties, and in particular, to the inverse dielectric constant $\alpha \simeq \epsilon_\infty^{-1}$ [94,95]. Since the 2D screening is associated to a smaller dielectric constant, a larger α is therefore needed to obtain an improved description. The fundamental quasiparticle band gaps of monolayer $SrTiO_3$ are summarized in Table I. The DFT fundamental band gap is indirect, with the valence band maximum (VBM) at M and the conduction band minimum (CBM) at Γ, while the DFT direct gap is defined at Γ. Despite the strong effect of QP corrections, the $G_0W_0^{full}$ indirect and direct gaps are opened at the same k-points (Γ-M and Γ), and are equal to 4.514 eV and 3.870 eV, respectively. The small difference between the $G_0W_0^{full}$ and $G_0W_0^{diag}$ QP gaps is due to the different degree of hybridization of the CBM orbital. By contrast, bulk $SrTiO_3$ exhibits a decreased band gap (3.55 eV), as predicted by $G_0W_0^{diag}$ [11]. This band-gap reduction is in line with the typical trend when going from monolayer to the bulk structure [96,97]. A notable difference is, however, visible in the nature of the gap, which displays a pure p-d character in the bulk phase and involves the degenerate Ti-t_{2g} states at Γ [9]. This degeneracy is broken in the monolayer limit, and the band becomes substantially hybridized at Γ.

B. Optical and excitonic properties

The optical response of monolayer $SrTiO_3$ is dominated by excitonic effects. The direct optical gap is associated to a large excitonic binding energy of 0.93 eV (see Table I). Compared with ultrathin transition metal materials, the predicted value falls within a comparable range to the highest observed E_{xb} in transition metal dichalcogenides (TMD) [47,98,99] (∼0.8–0.9 eV for freestanding WS_2 and WSe_2 [47]) and MXenes (considering ∼0.8 eV for Zr_2CO_2 [100] and ∼0.7 eV for Sc_2CF_2 [101]). This value is roughly four times larger than the one estimated for the bulk phase (∼0.2050.240 eV [8,9,16]); this increase is a typical consequence of the decreased screening of 2D materials [48,49,77]. Moreover, several researchers proposed a screened hydrogen model which establishes an explicit dependence between E_{xb} and the 2D polarizability α_{2D} [100,102,103]; In clear contrast to the bulk case, the model considers (in the large polarizability regime) the binding energy independent of the exciton reduced effective mass. By extracting α_{2D} from the *ab initio* data and employing the model's equation $E_{xb}^{hyd.model} = 3e^2/4\pi\alpha_{2D}$ we obtain $E_{xb}^{hyd.model} = 1.02$ eV, in good agreement with our BSE

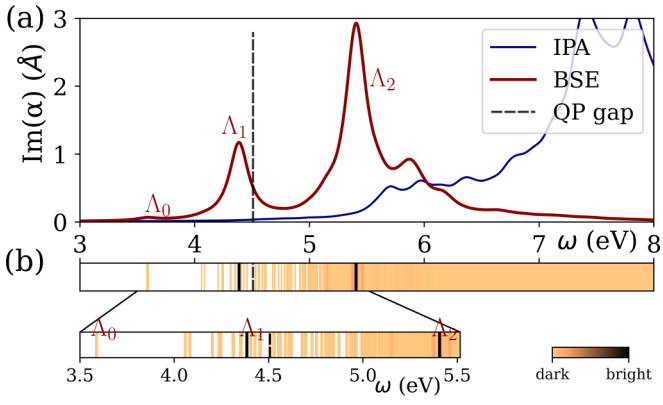

FIG. 2. (a) Imaginary part of 2D polarizabilities with excitonic effects (BSE) and in the independent particle approximation (IPA). The vertical dashed line represents the fundamental direct gap. The BSE eigenvalue spectrum is given in (b), with an insert zooming over the bound exciton region. The color coding indicates the associated oscillator strength with the maximum of the scale being set to that of Λ_2.

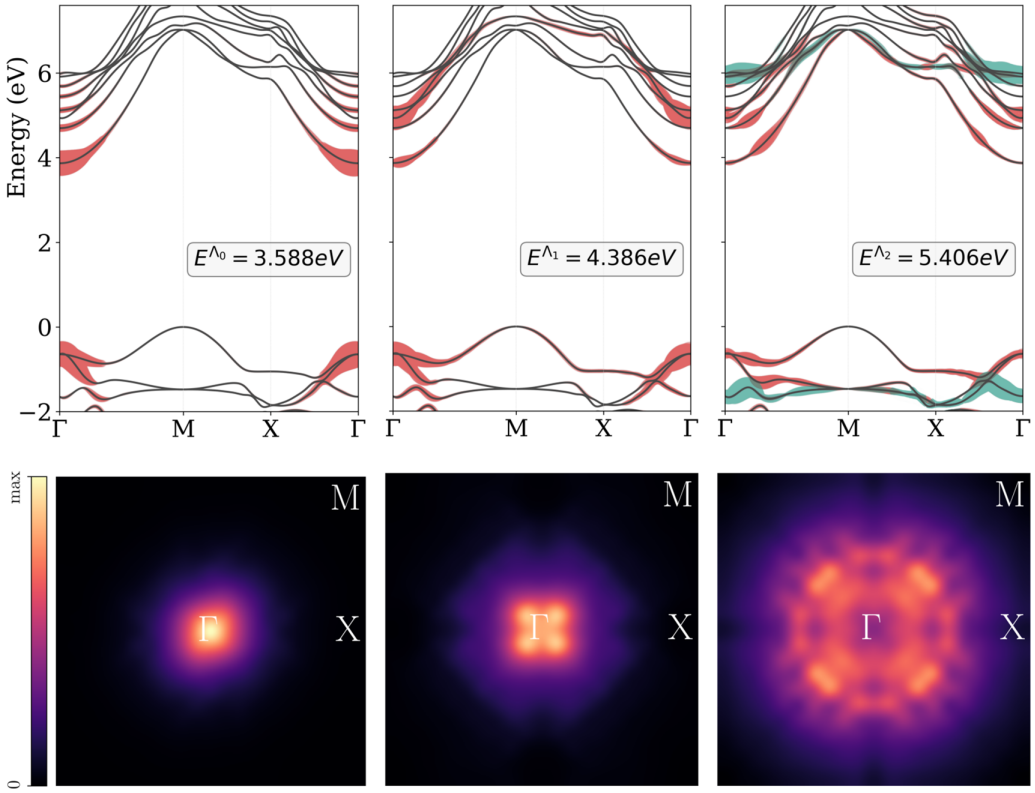

FIG. 3. Upper panels: Fatband analysis on the optical transitions associated with Λ_0, Λ_1, and Λ_2 states. The fatness of the bands is proportional to the square of the amplitude of the electron-hole coupling coefficients $|A^{\Lambda}_{\mathbf{k}vc}|^2$ with v, c, $\mathbf{k}$, and Λ denoting the valence band index, conduction band index, k-point, and BSE eigenvalue, respectively. For Λ_2, the O-$p \rightarrow$ Ti-d_{yz} + Ti-d_{xz} optical transitions, discussed in the text, are highlighted by a light blue color. Lower panels: Distribution of the BSE eigenvectors in the Brillouin zone for the corresponding BSE eigenvalues. The color coding denotes $\sum_{v,c} |A^{\Lambda}_{\mathbf{k}vc}|^2$.

prediction. The BSE-predicted imaginary part of the 2D polarizability in Fig. 2 is dominated by two very intense and narrow peaks. This is in marked contrast to the one computed from the independent particle approximation, which exhibits a long absorption tail. The first narrow peak is located below the QP direct gap and is determined by the excitonic state Λ_1. A low-intensity feature is visible at the optical direct gap and is associated to the lowest bound exciton Λ_0, with a considerable redshift at the onset energy of ∼1.0 eV. Λ_0 is related to a bright exciton, albeit with a very weak oscillator strength (less than 5% of Λ_1). The continuum region displays a single prominent structure, in the form of sharp peak (i.e., Λ_2 with the strongest oscillator strength) plus a shoulder. Now we turn to the analysis of the fine structure of bound excitons in Fig. 3. The lowest state Λ_0 is doubly degenerate and weakly optically active, with a modest oscillator strength. The contributions to the excitonic wave function in reciprocal space $A^{\Lambda_0}_{\mathbf{k}vc}$ are predominantly localized at Γ and originate from optical transitions from the valence O-p states the CBM. The low oscillator strength can be explained in terms of orbital characters of the CBM. Specifically, the conduction band minimum retains a substantial O-p and Sr hybridization; in particular, the Sr hybridization at Γ is mainly composed by Sr-s and Sr-p characters. This is, in turn, associated to a partial suppression of the optical matrix elements between the valence O-p states and the CBM. The major $A^{\Lambda_1}_{\mathbf{k}vc}$ terms correspond to interband transitions localized near Γ from the two highest valence bands formed by O-p_x/p_y states (doubly degenerate at Γ), to the second conduction band of Ti-d_{xy} character (see Fig. 3). The BSE eigenstate $A^{\Lambda_2}_{\mathbf{k}vc}$ in the continuum mixes the (previously cited) O-$p_x/p_y \rightarrow$ Ti-d_{xy} optical transitions with a second excitation channel (highlighted with a different color in Fig. 3), from the O-p_z valence states to the nondispersive conduction bands in the regions around Γ–X and Γ–M at ∼ 6.0 eV, dominated by Ti-d_{yz}/Ti-d_{xz} states (with a negligible hybridization with other states, less than 12%). The high intensity of the Λ_2 feature can be associated to the localization of the Ti-d states in the nondispersive regions at ∼ 6.0 eV. We note, moreover, that all O-p valence orbitals involved in Λ_1 and Λ_2 originate from the oxygen atoms situated in the Ti plane. Due to the particular screening environment of 2D compounds, the orbitals perpendicular to the monolayer plane (e.g., the ones involved in the O-$p_z \rightarrow$ Ti-d_{yz}/Ti-d_{xz} channel) experience a reduced screening with respect to the plane confined ones [104]; this effect concurs to explain the large ∼2.0–2.1 eV redshift of the Λ_2 peak. Next, we turn to the investigation of the excitonic dispersion at finite $\mathbf{q}$, that is beyond the optical limit. This allows us to further characterize and discriminate the excitonic properties in 2D systems [41,44,46,105,106]. The excitonic dispersion can be accessed experimentally by means of electron energy loss spectroscopy (EELS) or resonant inelastic x-ray spectroscopy (RIXS) [46]. In particular in the EELS technique the cross-section depends on the Loss function

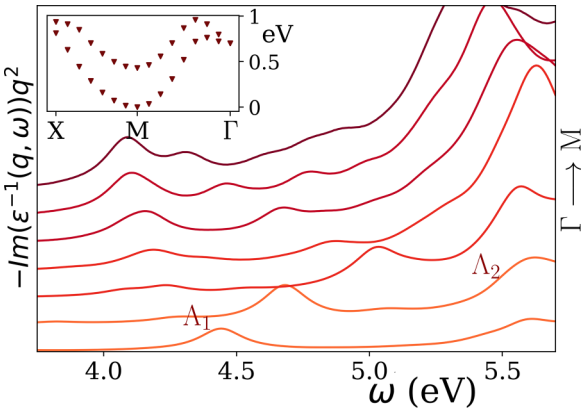

FIG. 4. Loss function for transferred momenta along the high-symmetry direction Γ-M, from $\mathbf{q} = M/8$ to $\mathbf{q} = M$. Each curve is multiplied by q^2, following Cudazzo and coworkers [46,105]. The insert shows the excitonic band structure for the lowest two excitons along X–M–Γ; the zero energy is set at the eigenvalues minimum at M.

$L(\mathbf{q}, \omega) = -\mathrm{Im}[\epsilon^{-1}(\mathbf{q}, \omega)]$. Our computed Loss functions for various $\mathbf{q}$ are plotted in Fig. 4 along Γ–M (corresponding to the indirect gap direction). It's interesting to find that the doubly degenerate lowest excitonic state Λ_0, that yields a low-intensity feature for $q \to 0$ becomes completely dark along Γ-M. Furthermore, the analysis of exciton dispersions (insert in Fig. 4) shows that the double-degeneracy is splitted away from Γ, and the two resulting excitonic bands reach their minimum at $\mathbf{q} = M$, in correspondence of the indirect QP band gap. The lowest (dark) excitonic band shows a parabolic dispersion around M, with an associated binding energy of 0.98 eV (at $\mathbf{q} = M$). Upon increasing momentum transfer, the peak associated with the Λ_1 state disperses to higher energies and progressively merges with the high-intensity structure at ∼5.5 eV (identifiable with the Λ_2 transition). At large $\mathbf{q}$ a new feature appears at transition energies around 4.1 eV, which originates from the interband transitions from the three highest valence bands to the lowest conduction band. In particular, for $\mathbf{q} = M$ a nonnegligible contribution to the BSE eigenstate $A_{vc\mathbf{k}}(\mathbf{q} = M)$ (up to 30% of the total spectral weight) is obtained by the transitions from valence O-p_z states, which are also involved in the Λ_2 excitonic transition.

IV. CONCLUSION

In summary, we investigated the quasiparticle and excitonic properties of freestanding monolayer $SrTiO_3$, using an *ab initio* approach based on many-body perturbation GW theory and Bethe-Salpeter equation. We demonstrate that the inclusion of off-diagonal self-energy matrix elements in the G_0W_0 scheme is crucial to correctly describe the strong hybridization of the lower conduction bands (which is wrongly accounted for by semi-local DFT) and hence prevents the appearance of unphysical dispersions. In the second part the excitonic properties both in the optical limit $\mathbf{q} \to 0$ and for finite momenta have been studied. We find that the spectra at $\mathbf{q} \to 0$ is dominated by excitonic effects, with a large binding energy of ∼0.93 eV at the direct optical gap. The analysis of the BS coupling components shows that the most intense peaks are originated from the O-$p \to$ Ti-d interband transitions, in conformity with the bulk description. In particular, the transitions from the in-plane O-p_x/p_y orbitals to Ti-d_{xy} orbitals and from out-of-plane O-p_z orbitals to Ti-d_{xz}/d_{yz} orbitals form separate excitation channels, which allows us to differentiate the two peaks. At finite $\mathbf{q}$, the lowest exciton becomes dark with a parabolic excitonic dispersion around the transition minimum at $\mathbf{q} = M$, an energy lower than the direct optical gap. Considering the enhanced excitonic features described in monolayer $SrTiO_3$, we anticipate this work will serve as a starting point to stimulate further studies on the optical properties of the other synthesized 2D perovskites and on the interplay between the excitonic interaction and the effects of strain and doping. Furthermore, the insights on the shortcomings of the semi-local and hybrid functionals reported in this work can provide a methodological reference when exploring the quasiparticle and optical properties of 2D TM perovskites.

ACKNOWLEDGMENTS

The authors thank G. Kresse, M. Marsili, and J. He for fruitful discussions. The computational results have been achieved using the Vienna Scientific Cluster (VSC) and the Galileo100 cluster (CINECA, LIMIT project).

[1] F. Dogan, H. Lin, M. Guilloux-Viry, and O. Peña, Focus on properties and applications of perovskites, Sci. Technol. Adv. Mater. **16**, 020301 (2015).

[2] X. Guan and L. Guo, Cocatalytic effect of $SrTiO_3$ on Ag_3PO_4 toward enhanced photocatalytic water oxidation, ACS Catal. **4**, 3020 (2014).

[3] Y. Liu, L. Xie, Y. Li, R. Yang, J. Qu, Y. Li, and X. Li, Synthesis and high photocatalytic hydrogen production of $SrTiO_3$ nanoparticles from water splitting under UV irradiation, J. Power Sources **183**, 701 (2008).

[4] S. Shoji, G. Yin, M. Nishikawa, D. Atarashi, E. Sakai, and M. Miyauchi, Photocatalytic reduction of CO_2 by Cu_xO nanocluster loaded $SrTiO_3$ nanorod thin film, Chem. Phys. Lett. **658**, 309 (2016).

[5] M. Betzinger, C. Friedrich, A. Görling, and S. Blügel, Precise response functions in all-electron methods: Application to the optimized-effective-potential approach, Phys. Rev. B **85**, 245124 (2012).

[6] C. E. Ekuma, M. Jarrell, J. Moreno, and D. Bagayoko, First principle electronic, structural, elastic, and optical properties of strontium titanate, AIP Adv. **2**, 012189 (2012).

[7] G. Cappellini, S. Bouette-Russo, B. Amadon, C. Noguera, and F. Finocchi, Structural properties and quasiparticle energies of

cubic SrO, MgO and $SrTiO_3$, J. Phys.: Condens. Matter **12**, 3671 (2000).

[8] L. Varrassi, P. Liu, Z. E. Yavas, M. Bokdam, G. Kresse, and C. Franchini, Optical and excitonic properties of transition metal oxide perovskites by the Bethe-Salpeter equation, Phys. Rev. Mater. **5**, 074601 (2021).

[9] L. Sponza, V. Véniard, F. Sottile, C. Giorgetti, and L. Reining, Role of localized electrons in electron-hole interaction: The case of $SrTiO_3$, Phys. Rev. B **87**, 235102 (2013).

[10] P. K. Gogoi, L. Sponza, D. Schmidt, T. C. Asmara, C. Diao, J. C. W. Lim, S. M. Poh, S. I. Kimura, P. E. Trevisanutto, V. Olevano, and A. Rusydi, Anomalous excitons and screenings unveiling strong electronic correlations in $SrTi_{1-x}$ Nb_x O_3 ($0 \leqslant x \leqslant 0.005$), Phys. Rev. B **92**, 035119 (2015).

[11] Z. Ergönenc, B. Kim, P. Liu, G. Kresse, and C. Franchini, Converged *GW* quasiparticle energies for transition metal oxide perovskites, Phys. Rev. Mater. **2**, 024601 (2018).

[12] A. Tröster, C. Verdi, C. Dellago, I. Rychetsky, G. Kresse, and W. Schranz, Hard antiphase domain boundaries in strontium titanate unravelled using machine-learned force fields, Phys. Rev. Mater. **6**, 094408 (2022).

[13] C. Verdi, L. Ranalli, C. Franchini, and G. Kresse, Quantum paraelectricity and structural phase transitions in strontium titanate beyond density functional theory, Phys. Rev. Mater. **7**, L030801 (2023).

[14] Z. Wang, Z. Zhong, X. Hao, S. Gerhold, B. Stöger, M. Schmid, J. Sánchez-Barriga, A. Varykhalov, C. Franchini, K. Held, and U. Diebold, Anisotropic two-dimensional electron gas at $SrTiO_3$(110), Proc. Natl. Acad. Sci. **111**, 3933 (2014).

[15] W. Meevasana, P. D. C. King, R. H. He, S.-K. Mo, M. Hashimoto, A. Tamai, P. Songsiriritthigul, F. Baumberger, and Z.-X. Shen, Creation and control of a two-dimensional electron liquid at the bare $SrTiO_3$ surface, Nat. Mater. **10**, 114 (2011).

[16] V. Begum, M. E. Gruner, and R. Pentcheva, Role of the exchange-correlation functional on the structural, electronic, and optical properties of cubic and tetragonal $SrTiO_3$ including many-body effects, Phys. Rev. Mater. **3**, 065004 (2019).

[17] D. Ji, S. Cai, T. R. Paudel, H. Sun, C. Zhang, L. Han, Y. Wei, Y. Zang, M. Gu, Y. Zhang, W. Gao, H. Huyan, W. Guo, D. Wu, Z. Gu, E. Y. Tsymbal, P. Wang, Y. Nie, and X. Pan, Freestanding crystalline oxide perovskites down to the monolayer limit, Nature (London) **570**, 87 (2019).

[18] S. S. Hong, J. H. Yu, D. Lu, A. F. Marshall, Y. Hikita, Y. Cui, and H. Y. Hwang, Two-dimensional limit of crystalline order in perovskite membrane films, Sci. Adv. **3**, eaao5173 (2017).

[19] L. Han, Y. Fang, Y. Zhao, Y. Zang, Z. Gu, Y. Nie, and X. Pan, Giant uniaxial strain ferroelectric domain tuning in freestanding $PbTiO_3$ films, Adv. Mater. Interfaces **7**, 1901604 (2020).

[20] A. G. Ricciardulli, S. Yang, J. H. Smet, and M. Saliba, Emerging perovskite monolayers, Nat. Mater. **20**, 1325 (2021).

[21] A. Chen, S. V. Nair, B. Miljkovic, C. Souza, H. E. Ruda, and Z. Ji, Electronic structure of bulk and two-dimensional $SrTiO_3$: DFT calculation with GGA + U methods, J. Nanopart. Res. **22**, 259 (2020).

[22] X.-B. Xiao and B.-G. Liu, Freestanding perovskite oxide monolayers as two-dimensional semiconductors, Nanotechnology **32**, 145705 (2021).

[23] S. Xu, F. Jia, S. Hu, A. Sundaresan, N. V. Ter-Oganessian, A. P. Pyatakov, J. Cheng, J. Zhang, S. Cao, and Wei Ren§, Predicting the structural, electronic and magnetic properties of few atomic-layer polar perovskite, Phys. Chem. Chem. Phys. **23**, 5578 (2021).

[24] B. Sohn, J. R. Kim, C. H. Kim, S. Lee, S. Hahn, Y. Kim, S. Huh, D. Kim, Y. Kim, W. Kyung, M. Kim, M. Kim, T. W. Noh, and C. Kim, Observation of metallic electronic structure in a single-atomic-layer oxide, Nat. Commun. **12**, 6171 (2021).

[25] Q. Li, J. Wu, T. Wu, H. Jin, N. Zhang, J. Li, W. Liang, M. Liu, L. Huang, and J. Zhou, Phase engineering of atomically thin perovskite oxide for highly active oxygen evolution, Adv. Funct. Mater. **31**, 2102002 (2021).

[26] X.-J. Hu, Y. Yang, C. Hou, and T.-X. Liang, Thermodynamic and electronic properties of two-dimensional $SrTiO_3$, J. Phys. Chem. C **126**, 517 (2022).

[27] Y. Zhou, S. Dong, C. Shan, K. Ji, and J. Zhang, Two-dimensional ferroelectricity induced by octahedral rotation distortion in perovskite oxides, Phys. Rev. B **105**, 075408 (2022).

[28] M. Campetella and M. Calandra, Polar magnetic metallic state in few-layer $BiFeO_3$, Phys. Rev. B **104**, 174111 (2021).

[29] C.-C. Chiu, S.-Z. Ho, J.-M. Lee, Y.-C. Shao, Y. Shen, Y.-C. Liu, Y.-W. Chang, Y.-Z. Zheng, R. Huang, C.-F. Chang, C.-Y. Kuo, C.-G. Duan, S.-W. Huang, J.-C. Yang, and Y.-D. Chuang, Presence of delocalized ti 3d electrons in ultrathin single-crystal $SrTiO_3$, Nano Lett. **22**, 1580 (2022).

[30] V. Harbola, S. Crossley, S. S. Hong, D. Lu, Y. A. Birkhölzer, Y. Hikita, and H. Y. Hwang, Strain gradient elasticity in $SrTiO_3$ membranes: Bending versus stretching, Nano Lett. **21**, 2470 (2021).

[31] B. Peng, R.-C. Peng, Y.-Q. Zhang, G. Dong, Z. Zhou, Y. Zhou, T. Li, Z. Liu, Z. Luo, S. Wang, Y. Xia, R. Qiu, X. Cheng, F. Xue, Z. Hu, W. Ren, Z.-G. Ye, L.-Q. Chen, Z. Shan, T. Min *et al.*, Phase transition enhanced superior elasticity in freestanding single-crystalline multiferroic $BiFeO_3$ membranes, Sci. Adv. **6**, eaba5847 (2020).

[32] G. Dong, S. Li, M. Yao, Z. Zhou, Y.-Q. Zhang, X. Han, Z. Luo, J. Yao, B. Peng, Z. Hu, H. Huang, T. Jia, J. Li, W. Ren, Z.-G. Ye, X. Ding, J. Sun, C.-W. Nan, L.-Q. Chen, J. Li *et al.*, Super-elastic ferroelectric single-crystal membrane with continuous electric dipole rotation, Science **366**, 475 (2019).

[33] Y. Xue, Y. Guo, and C. Geng, Functionalization of two-dimensional $PbTiO_3$ film by surface modification: A first-principles study, Appl. Surf. Sci. **563**, 150268 (2021).

[34] R. Xu, J. Huang, E. S. Barnard, S. S. Hong, P. Singh, E. K. Wong, T. Jansen, V. Harbola, J. Xiao, B. Y. Wang, S. Crossley, D. Lu, S. Liu, and H. Y. Hwang, Strain-induced room-temperature ferroelectricity in $SrTiO_3$ membranes, Nat. Commun. **11**, 3141 (2020).

[35] Y. Xue, C. Geng, and Y. Guo, Structural characterization and property modification for two-dimensional (001) $SrTiO_3$ nanosheets, Appl. Nanosci. **10**, 4273 (2020).

[36] Y. Sun, C. Yang, and J. Peng, 3D-strain-induced multiple semiconductormetallic phase transition in monolayer $SrTiO_3$, Appl. Phys. Lett. **122**, 023102 (2023).

[37] F. Jia, S. Xu, G. Zhao, C. Liu, and W. Ren, Structural and electronic properties of two-dimensional freestanding $BaTiO_3SrTiO_3$ heterostructures, Phys. Rev. B **101**, 144106 (2020).

[38] Y. Wang, P. Qian, Y. Liu, F. M. Zhang, H. L. Cai, X. S. Wu, and G. P. Zhang, Modulating the electronic and optical properties for $SrTiO_3/LaAlO_3$ bilayers treated as the 2D materials by biaxial strains, J. Phys.: Condens. Matter **32**, 215701 (2020).

[39] H. Haug and S. W. Koch, *Quantum Theory of the Optical and Electronic Properties of Semiconductors*, 5th ed. (World Scientific, Singapore, 2009).

[40] D. Y. Qiu, F. H. da Jornada, and S. G. Louie, Optical spectrum of MoS_2: Many-body effects and diversity of exciton states, Phys. Rev. Lett. **111**, 216805 (2013).

[41] L. Sponza, H. Amara, C. Attaccalite, S. Latil, T. Galvani, F. Paleari, L. Wirtz, and F. m. c. Ducastelle, Direct and indirect excitons in boron nitride polymorphs: A story of atomic configuration and electronic correlation, Phys. Rev. B **98**, 125206 (2018).

[42] D. Y. Qiu, F. H. da Jornada, and S. G. Louie, Screening and many-body effects in two-dimensional crystals: Monolayer MoS_2, Phys. Rev. B **93**, 235435 (2016).

[43] L. Yang, J. Deslippe, C.-H. Park, M. L. Cohen, and S. G. Louie, Excitonic effects on the optical response of Graphene and Bilayer Graphene, Phys. Rev. Lett. **103**, 186802 (2009).

[44] G. Fugallo, P. Cudazzo, M. Gatti, and F. Sottile, Exciton band structure of molybdenum disulfide: from monolayer to bulk, Electron. Struct. **3**, 014005 (2021).

[45] C. E. Ekuma, Optical absorption in monolayer SnO_2, Phys. Rev. B **99**, 075421 (2019).

[46] P. Cudazzo, L. Sponza, C. Giorgetti, L. Reining, F. Sottile, and M. Gatti, Exciton band structure in two-dimensional materials, Phys. Rev. Lett. **116**, 066803 (2016).

[47] G. Wang, A. Chernikov, M. M. Glazov, T. F. Heinz, X. Marie, T. Amand, and B. Urbaszek, *Colloquium:* Excitons in atomically thin transition metal dichalcogenides, Rev. Mod. Phys. **90**, 021001 (2018).

[48] F. Hüser, T. Olsen, and K. S. Thygesen, How dielectric screening in two-dimensional crystals affects the convergence of excited-state calculations: Monolayer MoS_2, Phys. Rev. B **88**, 245309 (2013).

[49] A. Chernikov, T. C. Berkelbach, H. M. Hill, A. Rigosi, Y. Li, B. Aslan, D. R. Reichman, M. S. Hybertsen, and T. F. Heinz, Exciton binding energy and nonhydrogenic rydberg series in monolayer WS_2, Phys. Rev. Lett. **113**, 076802 (2014).

[50] I. Guilhon, M. Marques, L. K. Teles, M. Palummo, O. Pulci, S. Botti, and F. Bechstedt, Out-of-plane excitons in two-dimensional crystals, Phys. Rev. B **99**, 161201(R) (2019).

[51] M. M. Ugeda, A. J. Bradley, S.-F. Shi, F. H. da Jornada, Y. Zhang, D. Y. Qiu, W. Ruan, S.-K. Mo, Z. Hussain, Z.-X. Shen, F. Wang, S. G. Louie, and M. F. Crommie, Giant band gap renormalization and excitonic effects in a monolayer transition metal dichalcogenide semiconductor, Nat. Mater. **13**, 1091 (2014).

[52] T. Mueller and E. Malic, Exciton physics and device application of two-dimensional transition metal dichalcogenide semiconductors, npj 2D Materials and Applications **2**, 29 (2018).

[53] J. Heyd, G. E. Scuseria, and M. Ernzerhof, Hybrid functionals based on a screened Coulomb potential, J. Chem. Phys. **118**, 8207 (2003).

[54] G. Kresse and J. Furthmüller, Efficient iterative schemes for ab initio total-energy calculations using a plane-wave basis set, Phys. Rev. B **54**, 11169 (1996).

[55] G. Kresse and J. Furthmüller, Efficiency of *ab initio* total energy calculations for metals and semiconductors using a plane-wave basis set, Comput. Mater. Sci. **6**, 15 (1996).

[56] P. E. Blöchl, Projector augmented-wave method, Phys. Rev. B **50**, 17953 (1994).

[57] G. Kresse and D. Joubert, From ultrasoft pseudopotentials to the projector augmented-wave method, Phys. Rev. B **59**, 1758 (1999).

[58] M. S. Hybertsen and S. G. Louie, Electron correlation in semiconductors and insulators: Band gaps and quasiparticle energies, Phys. Rev. B **34**, 5390 (1986).

[59] M. Shishkin and G. Kresse, Implementation and performance of the frequency-dependent *GW* method within the PAW framework, Phys. Rev. B **74**, 035101 (2006).

[60] M. Shishkin and G. Kresse, Self-consistent *GW* calculations for semiconductors and insulators, Phys. Rev. B **75**, 235102 (2007).

[61] M. Shishkin, M. Marsman, and G. Kresse, Accurate quasiparticle spectra from self-consistent *GW* calculations with Vertex Corrections, Phys. Rev. Lett. **99**, 246403 (2007).

[62] M. van Schilfgaarde, T. Kotani, and S. Faleev, Quasiparticle self-consistent *GW* theory, Phys. Rev. Lett. **96**, 226402 (2006).

[63] S. V. Faleev, M. van Schilfgaarde, and T. Kotani, All-electron self-consistent *GW* approximation: Application to Si, MnO, and NiO, Phys. Rev. Lett. **93**, 126406 (2004).

[64] L. Reining, The GW approximation: content, successes and limitations, WIREs Comput. Mol. Sci. **8**, e1344 (2018).

[65] M. J. van Setten, M. Giantomassi, X. Gonze, G.-M. Rignanese, and G. Hautier, Automation methodologies and large-scale validation for *GW*: Towards high-throughput *GW* calculations, Phys. Rev. B **96**, 155207 (2017).

[66] M. Stankovski, G. Antonius, D. Waroquiers, A. Miglio, H. Dixit, K. Sankaran, M. Giantomassi, X. Gonze, M. Côté, and G.-M. Rignanese, G^0W^0 band gap of ZnO: Effects of plasmon-pole models, Phys. Rev. B **84**, 241201(R) (2011).

[67] W. Gao, W. Xia, X. Gao, and P. Zhang, Speeding up GW calculations to meet the challenge of large scale quasiparticle predictions, Sci. Rep. **6**, 36849 (2016).

[68] P. Larson, M. Dvorak, and Z. Wu, Role of the plasmon-pole model in the GW approximation, Phys. Rev. B **88**, 125205 (2013).

[69] D. Sangalli, A. Ferretti, H. Miranda, C. Attaccalite, I. Marri, E. Cannuccia, P. Melo, M. Marsili, F. Paleari, A. Marrazzo, G. Prandini, P. BonfÃ , M. O. Atambo, F. Affinito, M. Palummo, A. Molina-Sánchez, C. Hogan, M. Grüning, D. Varsano, and A. Marini, Many-body perturbation theory calculations using the yambo code, J. Phys.: Condens. Matter **31**, 325902 (2019).

[70] A. Marini, C. Hogan, M. Grüning, and D. Varsano, yambo: An ab initio tool for excited state calculations, Comput. Phys. Commun. **180**, 1392 (2009).

[71] See Supplemental Material at http://link.aps.org/supplemental/10.1103/PhysRevMaterials.8.024001 for the full computations.

[72] M. Schlipf and F. Gygi, Optimization algorithm for the generation of ONCV pseudopotentials, Comput. Phys. Commun. **196**, 36 (2015).

[73] D. R. Hamann, Optimized norm-conserving Vanderbilt pseudopotentials, Phys. Rev. B **88**, 085117 (2013).

[74] G. Onida, L. Reining, and A. Rubio, Electronic excitations: density-functional versus many-body Green's-function approaches, Rev. Mod. Phys. **74**, 601 (2002).

[75] T. Sander, E. Maggio, and G. Kresse, Beyond the Tamm-Dancoff approximation for extended systems using exact diagonalization, Phys. Rev. B **92**, 045209 (2015).

[76] M. Gatti and F. Sottile, Exciton dispersion from first principles, Phys. Rev. B **88**, 155113 (2013).

[77] P. Cudazzo, I. V. Tokatly, and A. Rubio, Dielectric screening in two-dimensional insulators: Implications for excitonic and impurity states in graphane, Phys. Rev. B **84**, 085406 (2011).

[78] H. Pan, Y. Zhang, H. Jia, E. Cao, and Z. Yang, Electronic structures, stabilities, and magnetism of $SrTiO_3$ monolayer and ultrathin nanotubes, J. Supercond. Novel Magn. **34**, 2093 (2021).

[79] D. M. Juraschek and P. Narang, Highly confined phonon polaritons in monolayers of perovskite oxides, Nano Lett. **21**, 5098 (2021).

[80] R. D. King-Smith and D. Vanderbilt, Theory of polarization of crystalline solids, Phys. Rev. B **47**, 1651 (1993).

[81] P. Liu and C. Franchini, Advanced first-principle modeling of relativistic Ruddlesden—Popper Strontium iridates, Appl. Sci. **11**, 2527 (2021).

[82] D. Golze, M. Dvorak, and P. Rinke, The *GW* compendium: A practical guide to theoretical photoemission spectroscopy, Frontiers in Chemistry **7**, 377 (2019).

[83] K. Delaney, P. García-González, A. Rubio, P. Rinke, and R. W. Godby, Comment on "band-gap problem in semiconductors revisited: Effects of core states and many-body self-consistency", Phys. Rev. Lett. **93**, 249701 (2004).

[84] F. Fuchs, J. Furthmüller, F. Bechstedt, M. Shishkin, and G. Kresse, Quasiparticle band structure based on a generalized Kohn-Sham scheme, Phys. Rev. B **76**, 115109 (2007).

[85] J. Klimeš and G. Kresse, Kohn-Sham band gaps and potentials of solids from the optimised effective potential method within the random phase approximation, J. Chem. Phys. **140**, 054516 (2014).

[86] P. Aguado-Puente, S. Fahy, and M. Grüning, *GW* study of pressure-induced topological insulator transition in group-IV tellurides, Phys. Rev. Res. **2**, 043105 (2020).

[87] I. Aguilera, C. Friedrich, and S. Blügel, Many-body corrected tight-binding Hamiltonians for an accurate quasiparticle description of topological insulators of the Bi_2 Se_3 family, Phys. Rev. B **100**, 155147 (2019).

[88] I. Aguilera, C. Friedrich, G. Bihlmayer, and S. Blügel, *GW* study of topological insulators Bi_2 Se_3, Bi_2 Te_3, and Sb_2 Te_3: Beyond the perturbative one-shot approach, Phys. Rev. B **88**, 045206 (2013).

[89] D. Nabok, S. Blügel, and C. Friedrich, Electron–plasmon and electron–magnon scattering in ferromagnets from first principles by combining *GW* and *GT* self-energies, npj Comput. Mater. **7**, 178 (2021).

[90] M. van Schilfgaarde, T. Kotani, and S. V. Faleev, Adequacy of approximations in *GW* theory, Phys. Rev. B **74**, 245125 (2006).

[91] I. Aguilera, P. Palacios, and P. Wahnón, Understanding Ti intermediate-band formation in partially inverse thiospinel $MgIn_2S_4$ through many-body approaches, Phys. Rev. B **84**, 115106 (2011).

[92] M. Gatti, F. Bruneval, V. Olevano, and L. Reining, Understanding correlations in Vanadium dioxide from first principles, Phys. Rev. Lett. **99**, 266402 (2007).

[93] T. Förster, P. Krüger, and M. Rohlfing, *GW* calculations for Bi_2Te_3 and Sb_2Te_3 thin films: Electronic and topological properties, Phys. Rev. B **93**, 205442 (2016).

[94] J. H. Skone, M. Govoni, and G. Galli, Self-consistent hybrid functional for condensed systems, Phys. Rev. B **89**, 195112 (2014).

[95] P. Liu, C. Franchini, M. Marsman, and G. Kresse, Assessing model-dielectric-dependent hybrid functionals on the antiferromagnetic transition-metal monoxides MnO, FeO, CoO, and NiO, J. Phys.: Condens. Matter **32**, 015502 (2020).

[96] A. Chaves, J. G. Azadani, H. Alsalman, D. R. da Costa, R. Frisenda, A. J. Chaves, S. H. Song, Y. D. Kim, D. He, J. Zhou, A. Castellanos-Gomez, F. M. Peeters, Z. Liu, C. L. Hinkle, S.-H. Oh, P. D. Ye, S. J. Koester, Y. H. Lee, P. Avouris, X. Wang *et al.*, Band gap engineering of two-dimensional semiconductor materials, npj 2D Materials and Applications **4**, 29 (2020).

[97] J. Gusakova, X. Wang, L. L. Shiau, A. Krivosheeva, V. Shaposhnikov, V. Borisenko, V. Gusakov, and B. K. Tay, Electronic properties of bulk and monolayer TMDs: Theoretical study within DFT framework (GVJ-2e method), Phys. Status Solidi A **214**, 1700218 (2017).

[98] E. Jung, J. C. Park, Y.-S. Seo, J.-H. Kim, J. Hwang, and Y. H. Lee, Unusually large exciton binding energy in multilayered 2H-$MoTe_2$, Sci. Rep. **12**, 4543 (2022).

[99] A. Hanbicki, M. Currie, G. Kioseoglou, A. Friedman, and B. Jonker, Measurement of high exciton binding energy in the monolayer transition-metal dichalcogenides WS_2 and WSe_2, Solid State Commun. **203**, 16 (2015).

[100] Z. Jiang, Z. Liu, Y. Li, and W. Duan, Scaling universality between band gap and exciton binding energy of two-dimensional semiconductors, Phys. Rev. Lett. **118**, 266401 (2017).

[101] T. Ketolainen and F. Karlický, Optical gaps and excitons in semiconducting transition metal carbides (MXenes), J. Mater. Chem. C **10**, 3919 (2022).

[102] T. Olsen, S. Latini, F. Rasmussen, and K. S. Thygesen, Simple screened hydrogen model of excitons in two-dimensional materials, Phys. Rev. Lett. **116**, 056401 (2016).

[103] J.-H. Choi, P. Cui, H. Lan, and Z. Zhang, Linear scaling of the exciton binding energy versus the band gap of two-dimensional materials, Phys. Rev. Lett. **115**, 066403 (2015).

[104] H. Yu, M. Laurien, Z. Hu, and O. Rubel, Exploration of the bright and dark exciton landscape and fine structure of MoS_2 using G_0W_0 -BSE, Phys. Rev. B **100**, 125413 (2019).

[105] M. Bonacci, M. Zanfrognini, E. Molinari, A. Ruini, M. J. Caldas, A. Ferretti, and D. Varsano, Excitonic effects in graphene-like C_3N, Phys. Rev. Mater. **6**, 034009 (2022).

[106] D. Y. Qiu, T. Cao, and S. G. Louie, Nonanalyticity, valley quantum phases, and lightlike exciton dispersion in monolayer transition metal dichalcogenides: Theory and first-principles calculations, Phys. Rev. Lett. **115**, 176801 (2015).